

Article

Simple Loss Model of Battery Cables for Fast Transient Thermal Simulation

Emanuele Fedele , Luigi Pio Di Noia  and Renato Rizzo * 

Department of Electrical Engineering and Information Technology, Università di Napoli Federico II,
Via Claudio 21, 80125 Napoli, Italy

* Correspondence: renato.rizzo@unina.it

Abstract: In electric vehicles, currents with high-frequency ripples flow in the power cabling system due to the switching operation of power converters. Inside the cables, a strong coupling between the thermal and electromagnetic phenomena exists, since the temperature and Alternating Current (AC) density distributions in the strands affect each other. Due to the different time scales of magnetic and heat flow problems, the computational cost of Finite Element Method (FEM) numeric solvers can be excessive. This paper derives a simple analytical model to calculate the total losses of a multi-stranded cable carrying a Direct Current (DC) affected by a high-frequency ripple. The expression of the equivalent AC cable resistance at a generic frequency and temperature is derived from the general treatment of multi-stranded multi-layer windings. When employed to predict the temperature evolution in the cable, the analytical model prevents the use of complex FEM models in which multiple heat flow and magnetic simulations have to be run iteratively. The results obtained for the heating curve of a 35 mm² stranded cable show that the derived model matches the output of the coupled FEM simulation with an error below 1%, whereas the simple DC loss model of the cable gives an error of 2.4%. While yielding high accuracy, the proposed model significantly reduces the computational burden of the thermal simulation by a factor of four with respect to the complete FEM routine.

Keywords: cable; thermal analysis; skin and proximity effects; battery storage; ampacity



Citation: Fedele, E.; Di Noia, L.P.; Rizzo, R. Simple Loss Model of Battery Cables for Fast Transient Thermal Simulation. *Energies* **2023**, *16*, 2963. <https://doi.org/10.3390/en16072963>

Academic Editor: Simone Barcellona

Received: 22 February 2023

Revised: 15 March 2023

Accepted: 22 March 2023

Published: 23 March 2023



Copyright: © 2023 by the authors. Licensee MDPI, Basel, Switzerland. This article is an open access article distributed under the terms and conditions of the Creative Commons Attribution (CC BY) license (<https://creativecommons.org/licenses/by/4.0/>).

1. Introduction

Due to the ongoing effects of climate change, a significant reduction in greenhouse gas and pollutant emissions has become crucial. Such reduction demands a rapid transition from thermal to electrical transportation [1–7]. Electric vehicles require the use of onboard energy sources and storage systems such as fuel cells [8] and electrochemical batteries [9]. Battery electric vehicles are the most promising technology, although the actual electrochemical technology still needs improvements [10]. One of the main limitations to tackle is the reduction in volume and weight of battery cells so as to achieve higher values of specific power (kWh/kg) and power density (kWh/m³). To this aim, abundant research on promising chemistries for the electrode and electrolyte materials has been carried on in recent years [11–14]. Besides the inherent tradeoff between weight or volume and vehicle mileage, other technical issues associated with the correct management of the battery pack also exist. In fact, the use of a battery management system able to monitor the electrical and thermal behavior of the cells is mandatory, and optimized thermal management is of utmost importance to obtain a lighter and more compact battery pack for a given power rating [15]. Indeed, the removal of heat from the cells due to the flow of current and the internal entropy variation is one of the causes that lead to a reduction in the power density of the battery pack. The thermal behavior of electrochemical cells is widely studied in the literature, and numerical and model-based techniques have been proposed for the correct evaluation of the thermal state of the cells [16–19]. The correct performance of a battery

electric vehicle depends also on the proper operation of external devices attached to it, such as the DC/DC converters used as an interface to the electrical drives, the protection devices, and the wiring system [20]. The power cables play an important role in guaranteeing the vehicle's performance, especially from a reliability point of view [21,22]. In fact, due to the low volume availability and the non-negligible size of the cables, redundant wiring systems cannot be implemented onboard electric vehicles. Therefore, a failure of the main power cables between the battery pack and the propulsion system can rapidly lead to an unexpected stop of the electric vehicle. The damage and complete failure of power cables occur due to rapid degradation of the insulation, which can be caused by excessive electrical stress or overheating [23].

Virtually all the battery packs employed onboard EVs are interfaced with the traction and auxiliary loads through static power conversion stages. For this reason, the battery cabling system usually operates with distorted DC currents characterized by high-frequency ripples. Evaluating the thermal behavior of the cable in this condition is nontrivial, due to the mutual correlation between heat generation and electromagnetic phenomena, such as skin and proximity effects occurring in the conductor bundles [24,25]. On the other hand, the electrical power demanded by electric propulsion usually varies with fast dynamics determining sudden changes in the cable current, making transient analyses necessary. Complete numerical approaches based on the Finite Element Method (FEM) are often employed in the literature [26–30]; however, the high computation time required by the FEM simulations on a real multi-stranded cable geometry makes the method of application difficult for transient thermal simulations. The main idea of this paper is to derive a simple analytical model that provides a good estimation of the losses in high-power battery cables due to the flow of currents affected by high-frequency ripples. The model builds upon the premises of analytical equations known in the literature for the AC losses of round conductors in multi-layer transformer windings [31,32] and matches with good accuracy the results of electromagnetic and thermal FEM simulations. Thus, it can represent a fast and affordable means to evaluate the transient thermal behavior of the battery cabling system.

The remainder of this paper is organized as follows: Section 2 briefly introduces a typical battery EV powertrain architecture and its power cabling systems. Section 3 presents analytical loss models for multi-stranded cables carrying pure AC and distorted DC currents and provides a relation for the calculation of cable resistance at a generic temperature and frequency; in Section 4, the accuracy of the analytical loss models is assessed through the use of magnetic FEM simulations; in Section 5, a transient analysis of the cable heating is carried out using the simple method proposed in the paper and compared to that obtained by a full numerical routine comprising magnetic and thermal FEM simulations. Finally, Section 6 remarks on the methods and the results of the work and draws conclusions.

2. Battery Electric Vehicles Cabling System

Electric vehicles require an intensive adoption of power electronic converters, as they enable a flexible exchange of power between the battery pack, the propulsion motor drives, the auxiliary loads, and the onboard or offboard chargers. Figure 1 gives a sketch of a typical power circuit scheme of a battery EV, comprising the propulsion system and the onboard AC charger.

The DC/DC power converters play an important role in interfacing the battery pack with external power sources and loads. In fact, one DC/DC converter is often connected between the battery pack and the traction inverter to adapt the battery voltage to the level of the DC link and provide a stabilized voltage at the inverter input terminals. One more DC/DC converter is always included in the onboard charger to control the recharge of the battery pack from the external AC supply as prescribed by the charging profile and BMS limitations. As is well known, the operation of the power converters inevitably introduces some harmonic distortion in the currents and voltages of the power system and places extra stresses on every component of the drivetrain. For its part, the vehicle wiring system must

be designed to withstand a number of stress factors, namely, steep voltage transients at the motor terminals, high environmental temperatures, and non-negligible ripple content in the DC current drawn from the battery. As is clear from the circuit scheme, such high-frequency ripples are always present in the battery current, since power converters are operating during both propulsion and vehicle recharging.

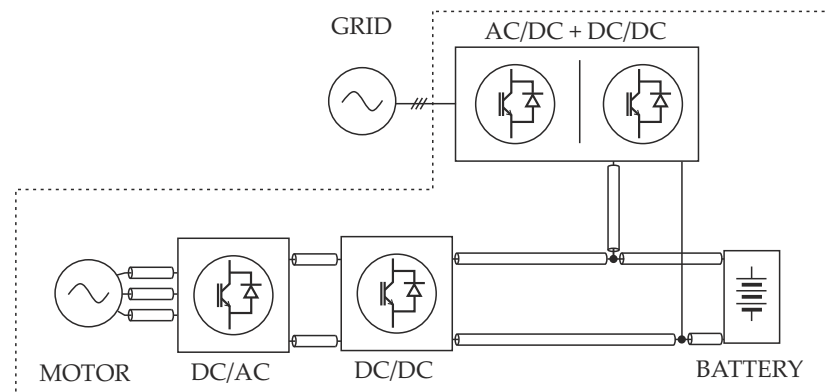


Figure 1. Typical EV power circuit including the propulsion system, the onboard charger, and the power cables.

For high-voltage EV applications, single-core multi-stranded high-temperature cables with PVC or silicon rubber insulation are usually employed in the DC stages of the propulsion system. The physical dimensions of the conductor core and insulation, as well as the nominal number of strands and their diameter for every standard cross-section, are prescribed by industry standards that cable makers are required to comply with [33,34]. Due to the multi-stranded geometry of power cables and the high-frequency harmonic of the battery current, additional Joule losses related to skin and proximity effects among strands can occur. Under particular ambient conditions, these extra Joule losses may cause excessive overheating, with a consequent fast degradation or even complete failure of the insulation layer. Therefore, an adequate evaluation of the cable's thermal behavior is of primary importance for the design and validation of the battery wiring system. In fact, a robust design can prevent accelerated aging, which can cause the intervention of protection devices or the fatal failure of the system, with consequent safety hazards [23].

3. Modeling of Cable Losses

3.1. Sinusoidal Current Waveform

The power dissipation per unit length P_0 of a round conductor subjected to an external magnetic field \vec{H} and carrying a sine current of amplitude I_0 at frequency f_0 can be expressed as [35]

$$P_0 = \frac{\rho I_0^2}{\sqrt{2}\pi\delta d_0} \psi_1(\Delta) - \sqrt{2} \frac{\pi\rho d_0}{\delta} H^2 \psi_2(\Delta) \quad (1)$$

where d_0 is the conductor diameter, ρ is the material resistivity, and δ is the skin depth, which is given by

$$\delta = \sqrt{\frac{\rho}{\pi\mu_0 f_0}} \quad (2)$$

In Equation (1), Δ is the normalized diameter with respect to the skin depth, i.e., $\Delta = d_0/\delta$, while $\psi_1(\Delta)$ and $\psi_2(\Delta)$ are functions of the real and imaginary parts of the k -th order Kelvin function $be_k(x)$ and their derivatives [36].

The geometry of a multi-stranded DC cable is schematized in Figure 2. Each strand is subjected to the magnetic field \vec{H} produced by the currents in all the other strands inside the cable. This field can be expressed in polar coordinates as

$$\vec{H}(r, \theta) = \frac{I}{2\pi r_c^2} r \hat{i}_\theta \tag{3}$$

where I is the total current carried by the cable, and r_c is the total radius of the cable.

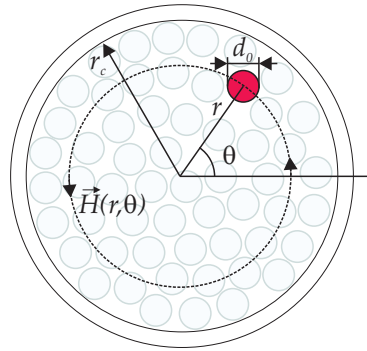


Figure 2. Multi-stranded cable geometry.

By denoting with N_0 the number of strands, the power loss density per unit volume of the cable can be expressed as

$$p = \frac{N_0 P_0}{\pi r_c^2} \tag{4}$$

By introducing the packing factor β ,

$$\beta = \frac{N_0 r_0^2}{r_c^2} \tag{5}$$

and using Equations (1) and (4), the power loss density rewrites as

$$p(r, \theta) = P_0 \frac{\beta}{\pi r_0^2} = \frac{I_0^2 \rho \beta}{2\sqrt{2}\pi^2 \delta r_0^3} \psi_1(\Delta) - 2\sqrt{2} \frac{\rho \beta}{\delta r_0} H^2 \psi_2(\Delta) \tag{6}$$

By integrating Equation (6) over the entire cable cross-section, the total AC power losses per unit length of the cable can be obtained:

$$\begin{aligned} P &= \int_0^{2\pi} \int_0^{r_c} \left(\frac{I_0^2 \rho \beta}{2\sqrt{2}\pi^2 \delta r_0^3} \psi_1(\Delta) - 2\sqrt{2} \frac{\rho \beta}{\delta r_0} H^2 \psi_2(\Delta) \right) dr d\theta \\ &= \frac{\rho I^2}{\sqrt{2}\pi \delta N_0 d_0} [\psi_1(\Delta) - \beta N_0 \psi_2(\Delta)] \end{aligned} \tag{7}$$

The above result differs from the usual expression of AC losses in multi-stranded multi-layer transformer windings [32,36] and is peculiar to multi-stranded power cables in which, differently from transformer windings, the external leakage magnetic field can be considered of negligible magnitude. From Equation (7), the AC equivalent resistance of the cable can be derived straightforwardly as

$$R_{AC} = \frac{P}{I^2/2} = \frac{\sqrt{2}\rho}{\pi \delta N_0 d_0} [\psi_1(\Delta) - \beta N_0 \psi_2(\Delta)] \tag{8}$$

Since the DC resistance per unit length of the cable is simply equal to the ratio between the resistivity and the cross-section,

$$R_{DC} = \frac{4\rho}{N_0\pi d_0^2} \quad (9)$$

the AC to DC resistance ratio k_R is equal to

$$k_R = \frac{R_{AC}}{R_{DC}} = \frac{\Delta}{2\sqrt{2}} [\psi_1(\Delta) - \beta N_0 \psi_2(\Delta)] \quad (10)$$

By recalling that the following Taylor series expansions hold true for $\psi_1(\Delta)$ and $\psi_2(\Delta)$,

$$\psi_1(\Delta) = 2\sqrt{2} \left(\frac{1}{\Delta} + \frac{1}{3 \cdot 2^8} \Delta^3 - \frac{1}{3 \cdot 2^{14}} \Delta^5 + \dots \right) \quad (11a)$$

$$\psi_2(\Delta) = \frac{1}{\sqrt{2}} \left(-\frac{1}{2^5} \Delta^3 + \frac{1}{2^{12}} \Delta^7 + \dots \right) \quad (11b)$$

and considering the terms up to the third power of Δ , the ratio k_R can be ultimately rewritten as

$$k_R = \frac{\Delta}{2\sqrt{2}} \left[2\sqrt{2} \left(\frac{1}{\Delta} + \frac{1}{3 \cdot 2^8} \Delta^3 \right) + \beta N_0 \frac{1}{\sqrt{2}} \frac{1}{2^5} \Delta^3 \right] = 1 + \frac{1 + 6\beta N_0}{3 \cdot 2^8} \Delta^4 \quad (12)$$

Substituting Equation (12) into Equation (10) yields the ultimate expression for the AC cable resistance at frequency f_0 :

$$R_{AC} = \frac{4\rho}{N_0\pi d_0^2} \left[1 + \frac{1 + 6\beta N_0}{3 \cdot 2^8} \Delta^4 \right] \quad (13)$$

where the dependency on frequency is not explicit but contained in the normalized skin depth Δ .

3.2. Generic Current Waveform

The above analysis can be extended to a generic periodic current waveform with DC and AC components, as typically encountered in electrical drive systems such as an EV powertrain. An arbitrary periodic current waveform of fundamental frequency f_0 can be expressed by means of its Fourier series expansion as

$$i(t) = I_{DC} + \sum_{h=1}^{+\infty} \sqrt{2} I_h \sin(2\pi h f_0 t - \phi_h) \quad (14)$$

where the closed-form expression of I_h and ϕ_h for numerous waveforms often encountered in power electronic applications can be found in the literature. The Joule losses corresponding to such arbitrary current waveforms are then given by

$$P = R_{DC} I_{DC}^2 + \sum_{h=1}^{+\infty} R_{AC}^{(h)} I_h^2 = R_{DC} \left(I_{DC}^2 + \sum_{h=1}^{+\infty} k_R^{(h)} I_h^2 \right) \quad (15)$$

where $R_{AC}^{(h)}$ and $k_R^{(h)}$ represent the AC cable resistance at frequency $h f_0$ and its normalized value, respectively. The normalized strand diameter at frequency $h f_0$ is equal to

$$\Delta_h = \frac{d_0}{\delta_h} = \frac{d_0}{\sqrt{1/\rho\pi\mu_0 h f_0}} = \sqrt{h} \Delta \quad (16)$$

from which the following expression for $k_R^{(h)}$ is derived:

$$k_R^{(h)} = \frac{\sqrt{h}\Delta}{2\sqrt{2}} \left[\psi_1(\sqrt{h}\Delta) - \beta N_0 \psi_2(\sqrt{h}\Delta) \right] \quad (17)$$

By recalling the Taylor series expansion provided in Equation (11a,b), Equation (17) rewrites as

$$k_R^{(h)} = 1 + \frac{1 + 6\beta N_0}{3 \cdot 2^8} h^2 \Delta^4 \quad (18)$$

The above expression is useful because it only requires the computation of the normalized skin depth at fundamental frequency f_0 . Equation (18) can be substituted into Equation (15) to calculate the total AC losses in the cable for a generic current waveform:

$$P = R_{DC} \left[I_{DC}^2 + \sum_{h=1}^{+\infty} \left(1 + \frac{1 + 6\beta N_0}{3 \cdot 2^8} \Delta^4 h^2 \right) I_h^2 \right] \quad (19)$$

4. Validation with Magnetic FEM Solver

The analytical expression of the AC cable resistance given by Equation (13) is validated against the results of the 2D Finite Element Method (FEM) software FEMM 4.2. The software solves the following phasor equation for the complete multi-stranded wire geometry:

$$\nabla \times \left(\frac{1}{\mu(B)} \nabla \times \mathbf{A} \right) = -j \frac{\omega}{\rho} \mathbf{A} + \mathbf{J}_s - \frac{1}{\rho} \nabla V \quad (20)$$

where \mathbf{A} and \mathbf{J}_s are the phasors of the magnetic induction vector potential and source current density, respectively. Several simulations are carried out for different frequencies and temperatures. This is necessary because the temperature affects the conductor resistivity ρ , which in turn influences the AC resistance, both directly through the resistivity temperature coefficient and indirectly through the skin depth. The comparison is carried out on a 35 mm² high-temperature DC cable for automotive applications whose main parameters are reported in Table 1.

Table 1. Cable parameters.

Parameter	Value
Conductor material	Copper
Nominal section	35 mm ²
Strand diameter	0.41 mm
Number of strands	276
Ampacity	280 A at 125 °C
Insulation material	Silicon rubber
Insulation thickness	1.04 mm
Temperature range	−40 °C to +180 °C

The current density distribution inside the individual cable strands as computed by the FEM solver at 280 A, 20 °C, and for a frequency of 5 kHz and 50 kHz is shown in Figure 3.

The FEM results show how the impact of skin and proximity effects on the current density distribution differs between the two cases. At a frequency of 5 kHz, the skin depth of copper at 20 °C is 0.92 mm, approximately two times the diameter of the strands. For this reason, the current density distribution is not far from being uniform and has peaks of 9 A/mm². On the other hand, the skin depth at 50 kHz lowers to 0.29 mm, approximately 0.71 times the strand diameter. Hence, the distribution of \mathbf{J} becomes much more nonuniform with maximum values of 48 A/mm², and higher Joule losses occur in the cable.

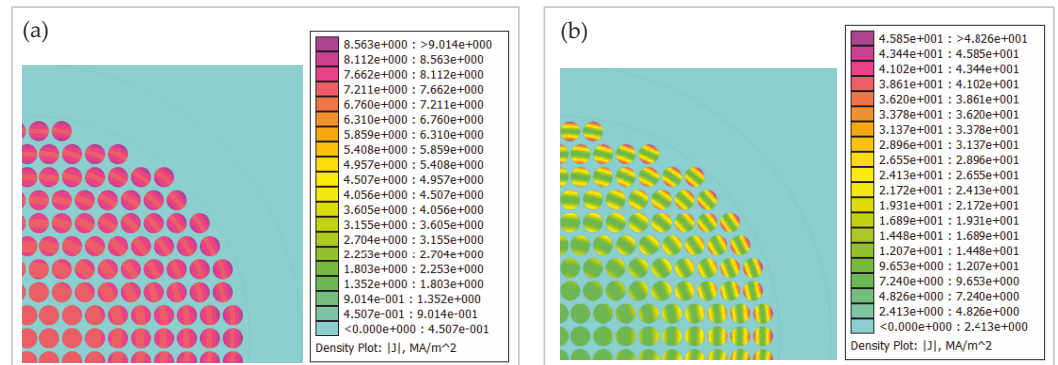


Figure 3. Current density in the cable at 20 °C and at a frequency of 5 kHz (a) and 50 kHz (b).

The AC equivalent resistance of the cable is evaluated in the post-processing phase based on the overall losses occurring in the conductor volume and the square of the current:

$$R_{AC} = \frac{\int_{V_c} \rho \|\mathbf{J}\|^2 dV}{1/2 \left(\int_{S_c} \|\mathbf{J}\| dS \right)^2} \quad (21)$$

where S_c and V_c are the cable cross section and volume, respectively. In Figure 4, the results of the FEM post-processing given by Equation (21) are compared with those given by the analytical Equation (13) for different frequencies and temperatures.

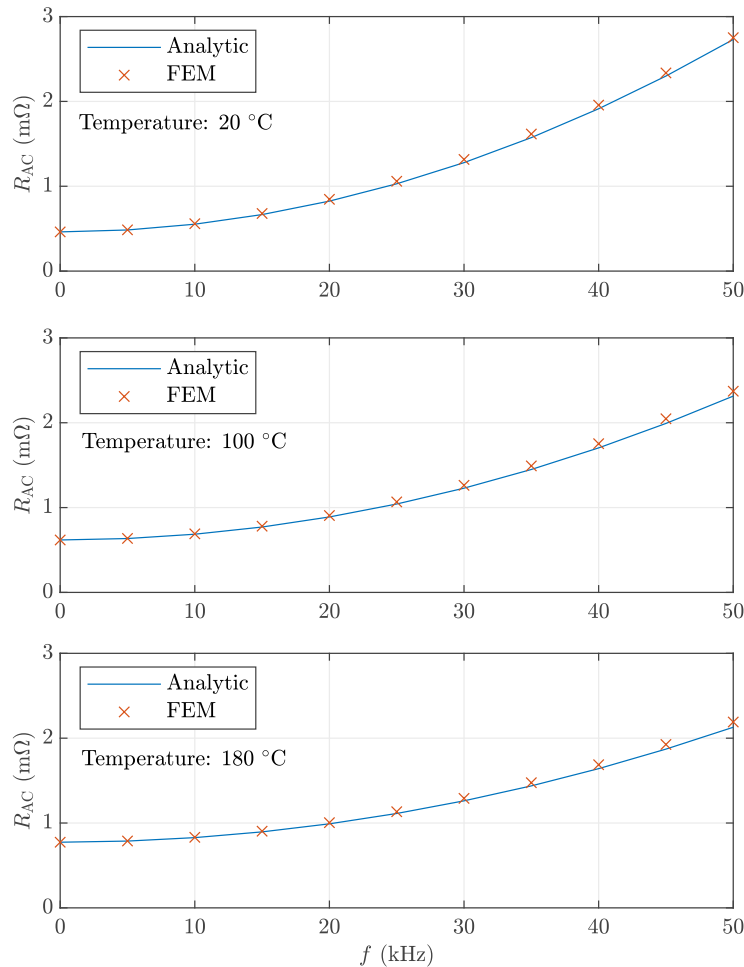


Figure 4. Comparison between analytic and FEM-calculated AC resistances at different frequencies and temperatures.

As can be seen, the analytical AC resistance equation matches with high accuracy the FEM results and proves effective in modeling the high-frequency skin and proximity effects in the strands and their complex dependency on temperature. Indeed, it is worth remarking that a higher temperature determines an increase in resistance at DC and low frequencies, but a reduction in resistance at high frequencies due to the increase in the skin depth. This is the reason why the cable has a higher resistance at 20 °C than at 180 °C at 50 kHz. The analytical model properly captures this opposite behavior at low and high frequencies.

5. Application to Thermal Transient Analysis

Thermal calculations of multi-stranded cables in free air require careful consideration of the mutual couplings between electromagnetic and thermal field problems [37]. In fact, the temperature inside the strands influences the resistivity and thus the magnetic field and current density distributions, which in turn determine the power losses inside the cable and its temperature evolution. While FEM analysis also proves effective in the thermal domain, the coupling between electromagnetic and thermal fields adds considerable computational costs, as the time scales of the two problems differ significantly [38]. If a generic current waveform is considered with multiple harmonic frequency magnetic problems, the computational burden of a fully coupled FEM model can become excessive. The practical benefit of using the analytical model of the total cable losses is therefore evaluated with application to the transient thermal analysis of the 35 mm² cable introduced in the previous section. A triangular current waveform is considered, which corresponds to the operation of a DC/DC converter attached to the battery. With reference to the Fourier series expansion in Equation (14), the following relations apply for a triangular shape [39]:

$$I_h = \frac{\Delta i}{d(1-d)\pi^2} \frac{\sin(h\pi d)}{h^2} \quad (22a)$$

$$\phi_h = -h\pi d \quad (22b)$$

where Δi is the peak-to-peak current ripple and d is the duty ratio.

The flowchart of the cross-coupled FEM simulation of the thermal transient is depicted in Figure 5.

For the triangular current at fundamental frequency f_0 , the first N_h harmonics shall be considered. At time step k , the temperature distribution inside the strands is used to solve N_h FEM magnetic problems at peak current $\sqrt{2}I_h$ and frequency hf_0 . The losses due to the harmonic currents are added to the DC losses and passed as input to the FEM thermal model that solves the heat flow equations and updates the temperature distribution, which is then used as the initial state of the subsequent iteration. Given N_t steps over the entire thermal simulation, $N_t \times N_h$ magnetic problems plus N_t thermal problems must be solved by two dedicated FEM routines.

On the other hand, the analytical loss model does not need N_h magnetic problems to be solved at each time step of the thermal simulation, reducing the total number of FEM calculations to N_t . In fact, at each time step, temperature θ is employed to calculate the DC resistance R_{DC} and normalized strand diameter Δ . These values are used by Equation (19) to evaluate the total Joule losses through a single computation. The total losses are then input to the thermal FEM solver to calculate the evolution of the temperature distribution.

The analysis was carried out for a current of 420 A of DC value (+50% with respect to the nominal ampacity) and 10% ripple. Natural convection on the external insulation surface at an air temperature of 60 °C is assumed. Matlab was employed to manage the iterative execution of electromagnetic and thermal simulations performed by FEMM 4.2 and for all the required pre- and post-processing calculations and plotting. Figure 6 shows the temperature distribution inside the cable as computed by the cross-coupled FEM routine after 10, 20, 30, and 40 min. As dictated by the circular symmetry of the problem, the heat flows from the core to the outer surface of the cable, and a temperature gradient of 10 to 20 °C is observed between the inner strands and the outer surface of the insulation layer.

After 40 min, the temperature in the silicon rubber has reached 193 °C, which is above the maximum continuous temperature rating due to a current higher than the rated ampacity.

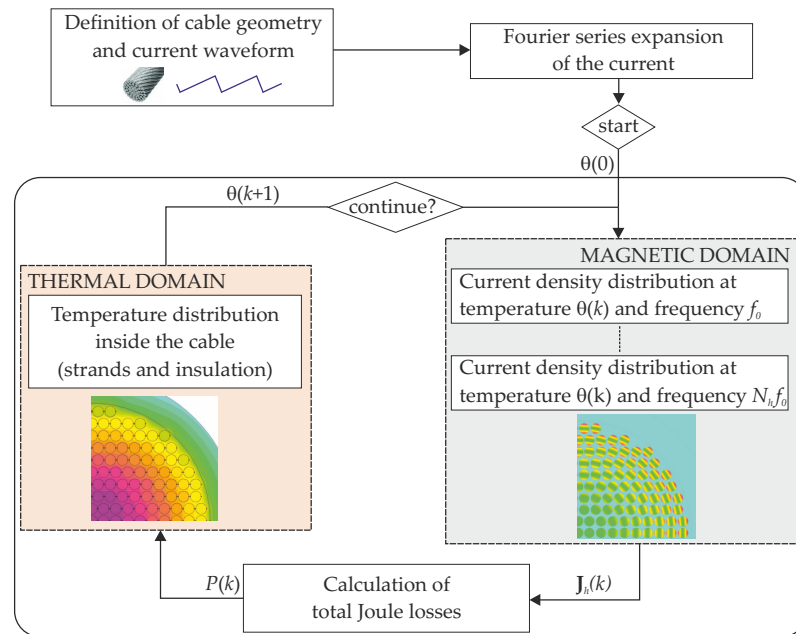


Figure 5. Flowchart for cross-coupled numerical evaluation of the cable thermal transient evolution.

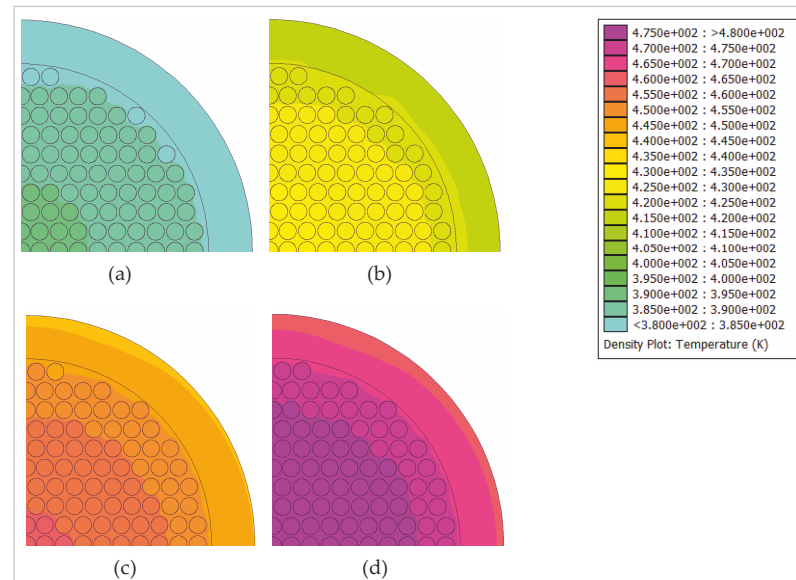


Figure 6. Temperature distribution inside the cable as computed by the coupled FEM routine after 10 min (a), 20 min (b), 30 min (c), and 40 min (d).

The variations in the average temperature of the strands and insulation as computed by the coupled FEM routine and analytical loss model are compared in Figure 7. In the plots, a third curve is also reported which represents the temperature evolution when only DC losses are considered, i.e., for $P = R_{DC} I_{DC}^2$.

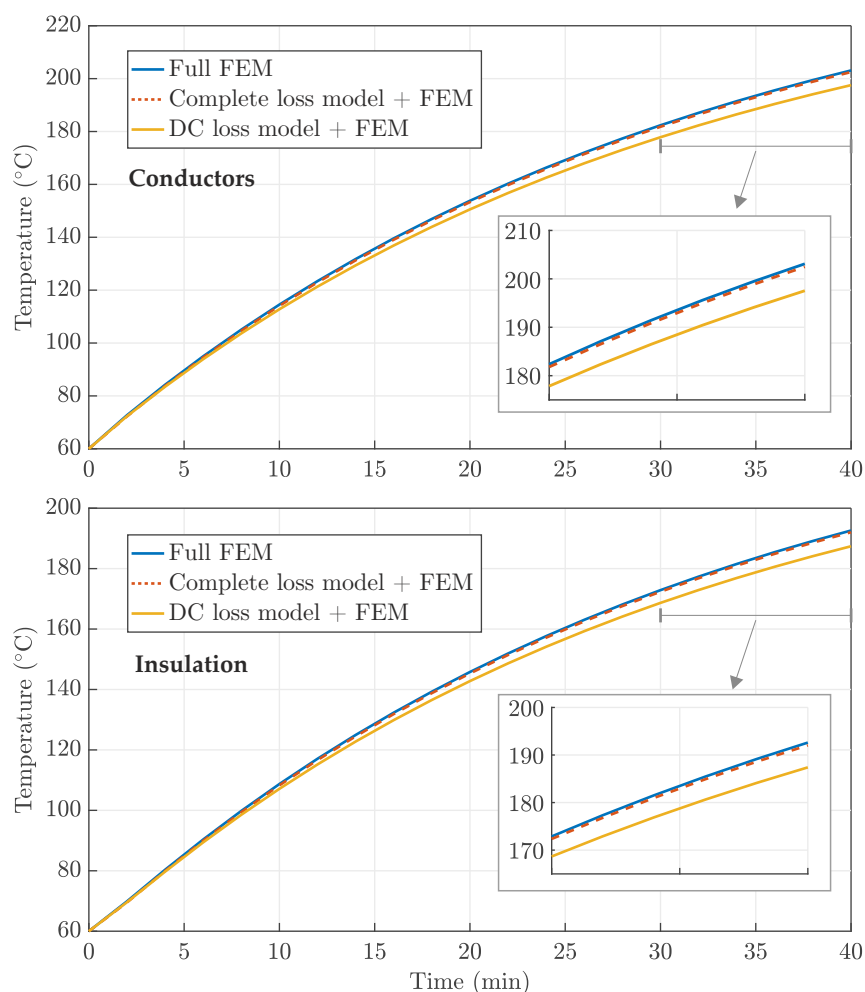


Figure 7. Temperature evolution in the conductors and insulations computed through different methods.

The comparison shows that the complete loss model accurately estimates the losses inside the cable and matches the thermal transient curve yielded by the complete FEM routine. However, it should be remarked that the coupled FEM simulation lasted approximately 17 h, while the one relying on the total loss analytical model lasted 4 h (both simulations were run on the same machine with 16 GB RAM and a six-core 3.10 GHz processor). On the other hand, the temperature profile obtained through the simple DC loss model is less accurate and presents an error that increases with the temperature. This increasing deviation can be explained as follows: The DC loss model underestimates the total cable resistance, which results in lower Joule losses and a consequently slower temperature increase. On the other hand, since the cable resistance increases with temperature (both in the DC and complete loss model), a slower temperature increase determines a slower increase in time of the internal losses. This inherent bidirectional coupling between temperature and power losses results in a discrepancy between the complete and DC loss model that increases with time. Based on the thermal constant of the cable here considered, this discrepancy becomes visible after 10 min. At the end of the simulation, the difference in the insulation temperature yielded by the two models amounts to 4.6 °C (2.4%). This discrepancy, while not excessive, suggests that the complete loss model given by Equation (19) may be preferred when a more precise evaluation of the cable temperature evolution under specific load or ambient conditions has to be performed. It is worth remarking that this higher accuracy is obtained at no additional cost, as the DC and complete loss models share the same negligible computational burden.

6. Conclusions

The DC cables connecting the battery pack to the traction system of an electric vehicle play an important role in guaranteeing the performance, reliability, and safety of the vehicle. The lifetime of a wiring system strongly depends on the temperature reached during operation. Many factors can affect the temperature of the cable, including the ambient conditions and the harmonic distortion in the current caused by the switching operation of power electronic converters attached to the battery. To evaluate the temperature evolution of DC cables under defined ambient and operating conditions, numerical approaches based on the Finite Element Method (FEM) represent the prevailing technique due to the versatility and accuracy of FEM solvers. In a multi-stranded cable geometry, which is usually found in battery power connections, a strong coupling between the thermal and electromagnetic phenomena exists, that is, they constitute a multi-physics problem. In fact, the temperature reached by the cable primarily depends on the Joule losses in the conductors, i.e., on the current density distribution within the strands. On the other hand, the distribution of harmonic AC current densities is affected by skin and proximity effects, whose impacts vary with frequency and temperature. Due to the very different time scales of magnetic and heat flow problems and the many harmonic components found in the current, a numerical solution to the problem can often be computationally hard.

This paper presented a simple analytical model to calculate the total losses occurring in a multi-stranded cable carrying a DC current that is affected by a high-frequency ripple. By considering the stranded geometry of the cable and the magnetic field inside it, the model can capture the joint effects of temperature and skin and proximity effects on the total Joule losses per unit length of the cable. The analytical equations describing the equivalent AC resistance of the cable at a fixed frequency and temperature were derived from the general treatment of high-frequency effects in multi-stranded multi-layer winding geometries and were validated against the results of time-harmonic FEM magnetic models. The model proved effective in matching with high accuracy the resistance values obtained through FEM analysis in the entire range of variation considered for frequency and temperature.

The effective advantage of using the proposed loss model to predict the temperature evolution inside the cable with a reduced computational burden was also assessed. Specifically, the output of a coupled electromagnetic–thermal FEM simulation comprising electromagnetic and heat flow calculations was compared to a simpler calculation routine, in which the loss density input to the heat flow FEM model was evaluated by means of the derived analytical loss model. The results showed that the temperature curve yielded by the simplified routine almost overlapped with that produced by the coupled FEM simulation. However, the simplified routine required only one-fourth of the computation time with respect to the full FEM simulation. On the other hand, the temperature evolution given by the simpler DC loss model was found to be affected by an error that increased with time and reached 2.4% at the end of the simulated time window. These results suggest that the proposed analytical modeling of total Joule losses in the multi-stranded cable can be of use when a more detailed evaluation of the temperature is to be performed at a largely reduced computation cost.

Author Contributions: Conceptualization, E.F., L.P.D.N. and R.R.; methodology, E.F., L.P.D.N. and R.R.; software, E.F. and L.P.D.N.; validation, E.F. and L.P.D.N.; formal analysis, E.F.; investigation, E.F. and L.P.D.N.; resources, E.F. and L.P.D.N.; data curation, E.F.; writing—original draft preparation, E.F.; writing—review and editing, L.P.D.N. and R.R.; visualization, E.F.; supervision, L.P.D.N. and R.R.; project administration, R.R. All authors have read and agreed to the published version of the manuscript.

Funding: This research received no external funding.

Data Availability Statement: The data presented in this study are available on request from the corresponding author.

Conflicts of Interest: The authors declare no conflict of interest.

References

1. Husain, I.; Ozpineci, B.; Islam, M.S.; Gurpinar, E.; Su, G.J.; Yu, W.; Chowdhury, S.; Xue, L.; Rahman, D.; Sahu, R. Electric Drive Technology Trends, Challenges, and Opportunities for Future Electric Vehicles. *Proc. IEEE* **2021**, *109*, 1039–1059. [[CrossRef](#)]
2. Sanguesa, J.A.; Torres-Sanz, V.; Garrido, P.; Martinez, F.J.; Marquez-Barja, J.M. A Review on Electric Vehicles: Technologies and Challenges. *Smart Cities* **2021**, *4*, 372–404. [[CrossRef](#)]
3. Fedele, E.; Iannuzzi, D.; Del Pizzo, A. Onboard energy storage in rail transport: Review of real applications and techno-economic assessments. *IET Electr. Syst. Transp.* **2021**, *11*, 279–309. [[CrossRef](#)]
4. Sun, X.; Li, Z.; Wang, X.; Li, C. Technology Development of Electric Vehicles: A Review. *Energies* **2020**, *13*, 90. [[CrossRef](#)]
5. Brelje, B.J.; Martins, J.R. Electric, hybrid, and turboelectric fixed-wing aircraft: A review of concepts, models, and design approaches. *Prog. Aerosp. Sci.* **2019**, *104*, 1–19. [[CrossRef](#)]
6. Fang, S.; Wang, Y.; Gou, B.; Xu, Y. Toward Future Green Maritime Transportation: An Overview of Seaport Microgrids and All-Electric Ships. *IEEE Trans. Veh. Technol.* **2020**, *69*, 207–219. [[CrossRef](#)]
7. Del Pizzo, A.; Polito, R.M.; Rizzo, R.; Tricoli, P. Design criteria of on-board propulsion for hybrid electric boats. In Proceedings of the The XIX International Conference on Electrical Machines—ICEM 2010, Rome, Italy, 6–8 September 2010; pp. 1–6. [[CrossRef](#)]
8. Sorlei, I.S.; Bizon, N.; Thounthong, P.; Varlam, M.; Carcadea, E.; Culcer, M.; Iliescu, M.; Raceanu, M. Fuel Cell Electric Vehicles—A Brief Review of Current Topologies and Energy Management Strategies. *Energies* **2021**, *14*, 252. [[CrossRef](#)]
9. Deng, J.; Bae, C.; Denlinger, A.; Miller, T. Electric Vehicles Batteries: Requirements and Challenges. *Joule* **2020**, *4*, 511–515. [[CrossRef](#)]
10. Zhao, G.; Wang, X.; Negnevitsky, M. Connecting battery technologies for electric vehicles from battery materials to management. *iScience* **2022**, *25*, 103744. [[CrossRef](#)]
11. Nitta, N.; Wu, F.; Lee, J.T.; Yushin, G. Li-ion battery materials: Present and future. *Mater. Today* **2015**, *18*, 252–264. [[CrossRef](#)]
12. Balasankar, A.; Arthiya, S.E.; Ramasundaram, S.; Sumathi, P.; Arokiyaraj, S.; Oh, T.; Aruchamy, K.; Sriram, G.; Kurkuri, M.D. Recent Advances in the Preparation and Performance of Porous Titanium-Based Anode Materials for Sodium-Ion Batteries. *Energies* **2022**, *15*, 495. [[CrossRef](#)]
13. Julien, C.M.; Mauger, A.; Zaghbi, K.; Groult, H. Comparative Issues of Cathode Materials for Li-Ion Batteries. *Inorganics* **2014**, *2*, 132–154. [[CrossRef](#)]
14. Li, Q.; Xu, C.; Huang, B.; Yin, X. Rhombohedral $\text{Li}_{1+x}\text{YxZr}_{2-x}(\text{PO}_4)_3$ Solid Electrolyte Prepared by Hot-Pressing for All-Solid-State Li-Metal Batteries. *Materials* **2020**, *13*, 1719. [[CrossRef](#)] [[PubMed](#)]
15. Hamed, M.M.; El-Tayeb, A.; Moukhtar, I.; El Dein, A.; Abdelhameed, E.H. A review on recent key technologies of lithium-ion battery thermal management: External cooling systems. *Results Eng.* **2022**, *16*, 100703. [[CrossRef](#)]
16. Kleiner, J.; Stuckenberger, M.; Komsijska, L.; Endisch, C. Advanced Monitoring and Prediction of the Thermal State of Intelligent Battery Cells in Electric Vehicles by Physics-Based and Data-Driven Modeling. *Batteries* **2021**, *7*, 31. [[CrossRef](#)]
17. Piccirillo, F.; Bianco, N.; Di Noia, L.P.; Guerriero, P.; Iasiello, M. Analysis of the Thermal Behavior of Li-Ion Pouch Battery Cell—Part I: Finite Element Simulations Including the Entropic Coefficient. In Proceedings of the 2022 28th International Workshop on Thermal Investigations of ICs and Systems (THERMINIC), Dublin, Ireland, 28–30 September 2022; pp. 1–6. [[CrossRef](#)]
18. Hu, Y.; Yurkovich, S.; Guezennec, Y.; Yurkovich, B. Electro-thermal battery model identification for automotive applications. *J. Power Sources* **2011**, *196*, 449–457. [[CrossRef](#)]
19. Morganti, M.V.; Longo, S.; Tirovic, M.; Blaise, C.Y.; Forostovsky, G. Multi-Scale, Electro-Thermal Model of NMC Battery Cell. *IEEE Trans. Veh. Technol.* **2019**, *68*, 10594–10606. [[CrossRef](#)]
20. Aghabali, I.; Bauman, J.; Kollmeyer, P.J.; Wang, Y.; Bilgin, B.; Emadi, A. 800-V Electric Vehicle Powertrains: Review and Analysis of Benefits, Challenges, and Future Trends. *IEEE Trans. Transp. Electrif.* **2021**, *7*, 927–948. [[CrossRef](#)]
21. Wang, C.; Liu, L.; Hou, X.; Wang, J.; Qiu, B. Failure Analysis and Improvement of High Voltage Cable of Electric Vehicle Based on Pseudo Damage Equivalence. In *Proceedings of the China SAE Congress 2020: Selected Papers*; Springer: Singapore, 2022; pp. 467–480.
22. Grandvilllemin, J.; Chamagne, D.; Tiraby, C.; Glises, R. Ampacity of power bus bars for Hybrid-Electric or Electric Vehicles. In Proceedings of the 2008 IEEE Vehicle Power and Propulsion Conference, Harbin, China, 3–5 September 2008; pp. 1–6. [[CrossRef](#)]
23. Bukya, M.; Kumar, R.; Gupta, R.K. A study on safety issues and analytical evaluation of stresses for HVDC cable in electrical vehicle. *AIP Conf. Proc.* **2020**, *2294*, 040001. [[CrossRef](#)]
24. Dias, R.A.; Lira, G.R.S.; Costa, E.G.; Ferreira, R.S.; Andrade, A.F. Skin effect comparative analysis in electric cables using computational simulations. In Proceedings of the 2018 Simposio Brasileiro de Sistemas Eletricos (SBSE), Niteroi, Brazil, 12–16 May 2018; pp. 1–6. [[CrossRef](#)]
25. Rozegnał, B.; Albrechtowicz, P.; Mamcarz, D.; Rerak, M.; Skaza, M. The Power Losses in Cable Lines Supplying Nonlinear Loads. *Energies* **2021**, *14*, 1374. [[CrossRef](#)]
26. Karahan, M.; Kalenderli, O. Coupled Electrical and Thermal Analysis of Power Cables Using Finite Element Method. In *Heat Transfer*; Vikhrenko, V.S., Ed.; IntechOpen: Rijeka, Croatia, 2011; Chapter 9. [[CrossRef](#)]
27. Di Noia, L.P.; Rizzo, R. Thermal Analysis of Battery Cables for Electric Vehicles. In Proceedings of the 2020 2nd IEEE International Conference on Industrial Electronics for Sustainable Energy Systems (IESES), Cagliari, Italy, 1–3 September 2020; Volume 1, pp. 298–302. [[CrossRef](#)]

28. Enescu, D.; Colella, P.; Russo, A. Thermal Assessment of Power Cables and Impacts on Cable Current Rating: An Overview. *Energies* **2020**, *13*, 5319. [[CrossRef](#)]
29. Cirino, A.W.; Paula, H.D.; Mesquita, R.C.; Saraiva, E. Cable parameter variation due to skin and proximity effects: Determination by means of finite element analysis. In Proceedings of the 2009 35th Annual Conference of IEEE Industrial Electronics, Porto, Portugal, 3–5 November 2009. [[CrossRef](#)]
30. Goga, V.; Paulech, J.; Váry, M. Cooling of electrical Cu conductor with PVC insulation - Analytical, numerical and fluid flow solution. *J. Electr. Eng.* **2013**, *64*, 13. [[CrossRef](#)]
31. Ferreira, J. Improved analytical modeling of conductive losses in magnetic components. *IEEE Trans. Power Electron.* **1994**, *9*, 127–131. [[CrossRef](#)]
32. Dowell, P. Effects of eddy currents in transformer windings. *Proc. Inst. Electr. Eng.* **1966**, *113*, 1387. [[CrossRef](#)]
33. *LV 112; Electrical Cables for Motor Vehicles*. ISO: Geneva, Switzerland, 2005.
34. *ISO 6722; Road Vehicles—60 V and 600 V Single-Core Cables*. ISO: Geneva, Switzerland, 2006.
35. Lammeraner, J.; Stafl, M. *Eddy Currents*; Iliffe Books: London, UK, 1966.
36. Tourkhani, F.; Viarouge, P. Accurate analytical model of winding losses in round Litz wire windings. *IEEE Trans. Magn.* **2001**, *37*, 914375. [[CrossRef](#)]
37. Cywiński, A.; Chwastek, K. A Multiphysics Analysis of Coupled Electromagnetic-Thermal Phenomena in Cable Lines. *Energies* **2021**, *14*, 8. [[CrossRef](#)]
38. Hameyer, K.; Driesen, J.; De Gersem, H.; Belmans, R. The classification of coupled field problems. *IEEE Trans. Magn.* **1999**, *35*, 1618–1621. [[CrossRef](#)]
39. Kondrath, N.; Kazimierczuk, M. Inductor winding loss owing to skin and proximity effects including harmonics in non-isolated pulse-width modulated dc–dc converters operating in continuous conduction mode. *IET Power Electron.* **2010**, *3*, 989. [[CrossRef](#)]

Disclaimer/Publisher’s Note: The statements, opinions and data contained in all publications are solely those of the individual author(s) and contributor(s) and not of MDPI and/or the editor(s). MDPI and/or the editor(s) disclaim responsibility for any injury to people or property resulting from any ideas, methods, instructions or products referred to in the content.